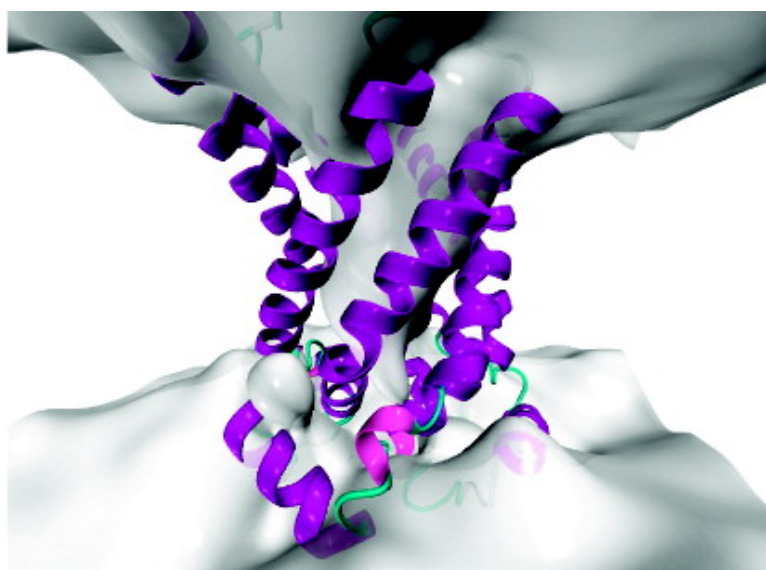


## Binding of ADP in the Mitochondrial ADP/ATP Carrier Is Driven by an Electrostatic Funnel

François Dehez, Eva Pebay-Peyroula, and Christophe Chipot

*J. Am. Chem. Soc.*, **2008**, 130 (38), 12725-12733 • DOI: 10.1021/ja8033087 • Publication Date (Web): 26 August 2008

Downloaded from <http://pubs.acs.org> on February 8, 2009



### More About This Article

Additional resources and features associated with this article are available within the HTML version:

- Supporting Information
- Links to the 1 articles that cite this article, as of the time of this article download
- Access to high resolution figures
- Links to articles and content related to this article
- Copyright permission to reproduce figures and/or text from this article

[View the Full Text HTML](#)

## Binding of ADP in the Mitochondrial ADP/ATP Carrier Is Driven by an Electrostatic Funnel

François Dehez,<sup>†</sup> Eva Pebay-Peyroula,<sup>‡</sup> and Christophe Chipot<sup>\*†</sup>

*Equipe de dynamique des assemblages membranaires, UMR No. 7565 CNRS-UHP, Nancy Université, BP 239, 54506 Vandœuvre-lès-Nancy cedex, France, and Institut de biologie structurale, UMR No. 5075 CEA-CNRS-UJF, 41, rue Jules Horowitz, 38027 Grenoble cedex 1, France*

Received May 4, 2008; E-mail: Christophe.Chipot@edam.uhp-nancy.fr

**Abstract:** The ADP/ATP carrier (AAC) is a membrane protein of paramount importance for the energy-fueling function of the mitochondria, transporting ADP from the intermembrane space to the matrix and ATP in the opposite direction. On the basis of the high-resolution, 2.2-Å structure of the bovine carrier, a total of 0.53  $\mu$ s of classical molecular dynamics simulations were conducted in a realistic membrane environment to decipher the early events of ADP<sup>3-</sup> translocation across the inner membrane of the mitochondria. Examination of *apo*-AAC underscores the impermeable nature of the carrier, impeding passive transport of permeants toward the matrix. The electrostatic funnel illuminated from three-dimensional mapping of the electrostatic potential forms a privileged passageway anticipated to drive the diphosphate nucleotide rapidly toward the bottom of the internal cavity. This conjecture is verified in the light of repeated, independent numerical experiments, whereby the permeant is dropped near the mouth of the mitochondrial carrier. Systematic association of ADP<sup>3-</sup> to the crevice of the AAC, an early event in its transport across the inner membrane, is accompanied by the formation of an intricate network of noncovalent bonds. Simulations relying on the use of an adaptive biasing force reveal for the first time that the proposed binding site corresponds to a minimum of the free energy landscape delineating the translocation of ADP<sup>3-</sup> in the carrier. The present work paves the way to the design of novel nucleotides and new experiments aimed at unveiling key structural features in the chronology of ADP/ATP transport across the mitochondrial membrane.

### Introduction

The mitochondrial ADP/ATP carrier (AAC) is an important constituent of the inner mitochondrial membrane, as it imports ADP and exports ATP toward the cytosol. AAC is related to the respiratory chain, which creates a proton gradient across the inner membrane, further utilized to catalyze the ATP synthesis from ADP and inorganic phosphate via the ATP synthetase. ATP is an essential molecule that provides chemical energy in most cellular reactions—a human being consumes its own weight of ATP per day. To fulfill these requirements, the cell machineries responsible not only for ATP synthesis but also for the transport of the substrates have to be very efficient. ADP<sup>3-</sup> and ATP<sup>4-</sup> are imported and exported, respectively, through the inner membrane by a very specific protein, the AAC. The outer mitochondrial membrane can be crossed through porin-like proteins in a somewhat less specific fashion.

Several energy-generating pathways are localized in the matrix of mitochondria (i.e., citric acid cycle and fatty acid oxidation), as well as other pathways (i.e., synthesis and degradation of amino acids). Heat generation is also triggered at the level of the inner mitochondrial membrane by dissipation of the proton gradient.<sup>1</sup> All these processes require the import

and export of metabolites or protons. In spite of large differences among these substrates, a common feature emerges: A variety of them are transported by carriers belonging to the same family, viz. the mitochondrial carrier family (MCF)—in the particular instance of protons, translocation is accomplished by uncoupling proteins (UCPs), which are specialized members of the MCF. The latter is characterized by a specific amino acid motif, Px<sub>n</sub>D/ExxK/RxK/R-(20–30 residues)-D/EGxxxxaK/RG, where “a” represents an aromatic residue, repeated three times in the sequence.<sup>2,3</sup> The triplication of about 100 amino acids including this motif most probably stems from an ancestral gene duplication.

Several pathologies involve such carriers.<sup>4</sup> Among all MCF carriers, the AAC is the most abundant in the membrane and represents up to 10% of the proteins that compose the inner membrane of bovine heart mitochondria. For these reasons, it was the first to be characterized.<sup>5,6</sup> In addition, two inhibitors, both acting as strong poisons by blocking nucleotide translocation,<sup>7,8</sup> were extensively utilized as tools for characterizing different conformational states of the carrier. On account of its

<sup>†</sup> Equipe de dynamique des assemblages membranaires, UMR No. 7565 CNRS-UHP, Nancy Université.

<sup>‡</sup> Institut de biologie structurale, UMR No. 5075 CEA-CNRS-UJF.

(1) Ricquier, D.; Casteilla, L.; Bouillaud, F. *FASEB J.* **1991**, *5*, 2237–2242.

(2) Walker, J. E.; Runswick, M. J. *J. Bioenerg. Biomembr.* **1993**, *25*, 435–446.

(3) Jezek, P.; Jezek, J. *FEBS Lett.* **2003**, *534*, 15–25.

(4) Palmieri, F. *Pflug. Arch.* **2004**, *447*, 689–709.

(5) Vignais, P. V. *Biochim. Biophys. Acta* **1976**, *456*, 1–38.

(6) Klingenberg, M. *Arch. Biochem. Biophys.* **1989**, *270*, 1–14.

(7) Vignais, P. V.; Vignais, P. V.; Stanislas, E. *Biochim. Biophys. Acta* **1962**, *60*, 284–300.

(8) Henderson, P. J.; Lardy, H. A. *J. Biol. Chem.* **1970**, *245*, 1319–1326.

abundance in natural sources, the structure of the AAC was also the first to be explored by electron microscopy<sup>9</sup> and X-ray crystallography. The AAC could be crystallized in the presence of the inhibitor carboxyatractyloside (CATR),<sup>10</sup> which is known to bind to the carrier from the intermembrane space (IMS), hampering ADP<sup>3-</sup> import.

The structure was solved to 2.2 Å resolution,<sup>11</sup> revealing for the first time the overall fold of MCF carriers and highlighting the role played by the MCF motif in the folding. Proline residues induce sharp kinks in three of the transmembrane (TM) helices, whereas the basic and acidic amino acids from the first part of the motif link these three helical segments together through salt bridges (see Supporting Information). The three salt bridges are located at the bottom of a large cavity opened toward the IMS, two of them having been already postulated on the basis of revertant studies.<sup>12</sup> The cavity is lined by four patches formed by basic residues, described to be important for the function (for a review of all the mutants and their implications, see ref 13). It contains three aligned tyrosine residues and possesses a slight constriction close to the bottom, consisting of four amino acids that are strictly conserved among ADP/ATP carriers.<sup>14</sup> Even though the position of many amino acids known to alter nucleotide transport could be highlighted, thereby shedding the first light on a putative mechanism, the structure of a single conformation alone does not answer fundamental questions about the access of ADP<sup>3-</sup> into the cavity, the selective recognition of ADP<sup>3-</sup> and ATP<sup>4-</sup>, as well as the structural modifications that allow the transport to occur. Unfortunately, blocking the carrier at key stages of the complete transport process in order to isolate intermediate states remains a daunting task. Inhibitors like CATR or bongkreikic acid (BA) have proven to constitute powerful tools, albeit, considering that they are chemically rather far from true nucleotides, they are admittedly of limited use. Solving structures that participate in the transport mechanism, therefore, require the synthesis of alternate nucleotide mimetics. This appealing strategy, pursued for other membrane proteins, e.g., calcium ATPase,<sup>15,16</sup> has helped pinpoint important intermediate states involved in their function. It is, therefore, becoming clear that, in order to reach the proposed goal, an improved knowledge of the structural and dynamic features of the carrier–nucleotide interaction is necessary.

The existence of a general transport mechanism among all MCF members remains also an open question. In addition, the structure determined by X-ray crystallography is monomeric, without any obvious interface conducive to strong dimerization.<sup>17</sup> Furthermore, the size of the cavity is sufficient to accommodate a nucleotide. On the basis of previous biochemical and functional experiments, it was almost admitted that MCF

carriers function as dimers. The three-dimensional structure of the carrier, however, casts doubt on this hypothesis. Recent contributions report that the AAC solubilized in detergents under different conditions is monomeric,<sup>18,19</sup> and that the yeast carrier is able to function as a monomer.<sup>20</sup>

The present research article addresses the first act of the transport mechanism, namely the entrance of ADP<sup>3-</sup> into the cavity and its subsequent association to putative binding sites. To reach this objective, molecular dynamics (MD) simulations were carried out over realistic time scales, based on the crystallographic structure of the mitochondrial carrier. To pinpoint possible structural modifications of the membrane protein upon transport of the diphosphate nucleotide, the AAC was examined both in its *apo* conformation and with 10 mM ADP and ATP. In addition, free energy calculations relying upon the knowledge of the average force exerted along a unidimensional construct of the reaction coordinate are employed to locate the possible binding sites of ADP<sup>3-</sup> in the carrier. Inferences drawn from the present set of simulations shed new light on the second stage of the transport mechanism, whereby ADP<sup>3-</sup> is imported into the matrix.

## Methods and Computational Details

**Molecular Assays.** In this contribution, two distinct assays were considered to model in a realistic environment the mitochondrial carrier in its *apo* form and with 10 mM ADP and ATP. The initial conformation of the AAC corresponds to PDB structure 1OKC, from which the specific inhibitor carboxyatractyloside (CATR) was removed. The carrier was subsequently inserted in a thermalized, fully hydrated palmitoyloleoylphosphatidylcholine (POPC) bilayer consisting of 228 lipid units in equilibrium with an aqueous phase formed by 10 553 water molecules. The net excess charge of *apo*-AAC was compensated by 18 chloride counterions. In the second assay featuring 10 mM ADP and ATP, i.e., 10 ADP<sup>3-</sup> and 10 ATP<sup>4-</sup>, the initial Cartesian coordinates of the carrier correspond to the end point of the simulation of *apo*-AAC. The di- and triphosphate nucleotides were placed initially on each side of the lipid bilayer, viz., on the intermembrane space side and on the matrix side, respectively. The additional negative charges of the ADP<sup>3-</sup> and ATP<sup>4-</sup> were balanced by 52 sodium counterions. The dimensions of the two assays after appropriate equilibration were ca. 84 × 75 × 97 Å<sup>3</sup>.

**MD Simulation.** All simulations were performed using the NAMD simulation package<sup>21</sup> in the isobaric–isothermal ensemble. The pressure and the temperature were fixed at 1 bar and 300 K, respectively, employing the Langevin piston algorithm<sup>22</sup> and softly damped Langevin dynamics. The molecular assays were replicated in the three directions of Cartesian space by means of periodic boundary conditions. The particle-mesh Ewald method<sup>23</sup> was employed to compute electrostatic interactions. The short-range Lennard-Jones potential was smoothly truncated. The *r*-RESPA multiple time-step propagator<sup>24</sup> was used to integrate the equations of motion with a time step of 2 and 4 fs for short- and long-

- (9) Kunji, E. R. S.; Harding, M. J. *Biol. Chem.* **2003**, *278*, 36985–36988.
- (10) Dahout-Gonzalez, C.; Brandolin, G.; Pebay-Peyroula, E. *Acta Crystallogr. D: Biol. Crystallogr.* **2003**, *59*, 2353–2355.
- (11) Pebay-Peyroula, E.; Dahout-Gonzalez, C.; Kahn, R.; Trézéguet, V.; Lauquin, G. J. M.; Brandolin, G. *Nature* **2003**, *426*, 39–44.
- (12) Nelson, D. R.; Felix, C. M.; Swanson, J. M. *J. Mol. Biol.* **1998**, *277*, 285–308.
- (13) Nury, H.; Dahout-Gonzalez, C.; Trézéguet, V.; Lauquin, G. J. M.; Brandolin, G.; Pebay-Peyroula, E. *Annu. Rev. Biochem.* **2006**, *75*, 713–741.
- (14) Pebay-Peyroula, E.; Brandolin, G. *Curr. Opin. Struct. Biol.* **2004**, *14*, 420–425.
- (15) Toyoshima, C.; Nomura, H.; Tsuda, T. *Nature* **2004**, *432*, 361–368.
- (16) Jensen, A. M. L.; Sørensen, T. L. M.; Olesen, C.; Møller, J. V.; Nissen, P. *EMBO J.* **2006**, *25*, 2305–2314.
- (17) Nury, H.; Dahout-Gonzalez, C.; Trézéguet, V.; Lauquin, G.; Brandolin, G.; Pebay-Peyroula, E. *FEBS Lett.* **2005**, *579*, 6031–6036.

- (18) Bamber, L.; Harding, M.; Butler, P. J. G.; Kunji, E. R. S. *Proc. Natl. Acad. Sci. U.S.A.* **2006**, *103*, 16224–16229.
- (19) Nury, H. *Études structurales du transporteur d'ADP/ATP*. Ph.D. thesis, Université Joseph Fourier, 2007.
- (20) Bamber, L.; Harding, M.; Monné, M.; Slotboom, D. J.; Kunji, E. R. S. *Proc. Natl. Acad. Sci. U.S.A.* **2007**, *104*, 10830–10834.
- (21) Phillips, J. C.; Braun, R.; Wang, W.; Gumbart, J.; Tajkhorshid, E.; Villa, E.; Chipot, C.; Skeel, L.; Kalé, R. D.; Schulten, K. *J. Comput. Chem.* **2005**, *26*, 1781–1802.
- (22) Feller, S. E.; Zhang, Y. H.; Pastor, R. W.; Brooks, B. R. *J. Chem. Phys.* **1995**, *103*, 4613–4621.
- (23) Darden, T. A.; York, D. M.; Pedersen, L. G. *J. Chem. Phys.* **1993**, *98*, 10089–10092.
- (24) Tuckerman, M. E.; Berne, B. J.; Martyna, G. J. *J. Phys. Chem. B* **1992**, *97*, 1990–2001.

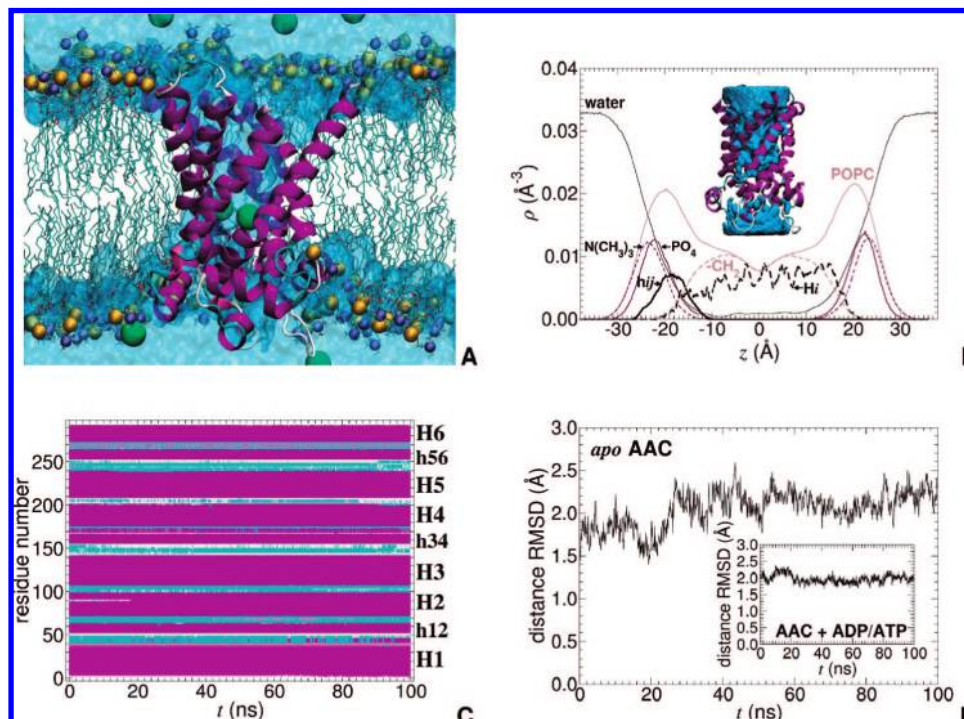


**Figure 1.** (A) *apo*-AAC in a fully hydrated POPC bilayer after 0.1  $\mu\text{s}$ . TM  $\alpha$ -helices are shown as purple ribbons. Chloride counterions are depicted as green van der Waals spheres. A semitransparent, continuous representation is used for water. Lipid units are featured as cyan rods, with their phosphate and choline groups depicted as orange and blue van der Waals spheres, respectively. The image rendering was done with VMD.<sup>41</sup> (B) Number density profiles of the molecular assembly averaged over the entire 0.1- $\mu\text{s}$  trajectory.  $H_i$  denotes the subset of TM  $\alpha$ -helices, whereas  $h_{ij}$  corresponds to the three short  $\alpha$ -helical stretches. Inset: Mass-weighted isodensity map of water in *apo*-AAC averaged over the 0.1- $\mu\text{s}$  trajectory and highlighting the absence of conduction between the matrix and the intermembrane space of the mitochondria. (C) Time evolution of the secondary structure of *apo*-AAC.  $\alpha$ - and  $3_{10}$ -helices, coils, and turns are highlighted in purple, pink, white, and cyan, respectively. (D) Time evolution of the distance rmsd over the backbone atoms forming *apo*-AAC with respect to the crystallographic structure.<sup>11</sup>

range forces, respectively. Covalent bonds involving a hydrogen atom were constrained to their equilibrium length by means of the Rattle algorithm.<sup>25</sup> The mitochondrial AAC and its environment were described by the all-atom CHARMM27 force field.<sup>26,27</sup> Each assay, i.e., the AAC in its *apo* form or with 10 mM ADP and ATP, was run over a period of 0.1  $\mu\text{s}$  after proper equilibration. To appraise the propensity of the permeant to reach in a systematic fashion a putative binding site located at the bottom of the internal cavity, seven additional, shorter simulations of the second assay were carried out, assigning different sets of initial positions and momenta to an ADP molecule dropped near the mouth of the carrier. These different numerical experiments of duration equal to 17.5, 77, 41, 42, 5.3, 3.6, and 20 ns correspond to a total simulation time of ca. 0.21  $\mu\text{s}$ . Running on the 16 cores of an array of two 2.33-GHz Intel Xeon QC processors communicating via a low-latency Infiniband network, the wall clock time was equal to 0.62 day per nanosecond.

**Free Energy Calculations.** To investigate the transport of ADP in the cavity of the mitochondrial AAC, a surrogate reaction coordinate was defined as the distance separating the center of mass of the permeant from the centroid of the lower region of helices H1, H3, and H5, i.e., below the hinges formed by the triplet of proline residues P27, P132, and P229, projected onto the  $z$ -direction of Cartesian space. Variation of the free energy,  $\Delta G(z)$ , along  $z$  was determined using the ABF method,<sup>28</sup> which relies upon the integration of the average force acting in the direction of  $z$ . In the NAMM implementation of ABF,<sup>29</sup> this force is determined within

the classical thermodynamic integration formalism.<sup>30</sup> The free energy derivative,  $dG(z)/dz$ , is estimated locally as the simulation progresses, thereby providing a continuous update of the biasing force. When applied to the system, this bias generates a Hamiltonian exempt of a net average force along  $z$ . As a result, all values of the model reaction coordinate are sampled with an equal probability, thus improving markedly the accuracy of the computed free energies. Notably, this method makes no *a priori* assumptions about the final state of the transformation but rather allows the permeant to diffuse freely along the postulated model reaction coordinate. The interval spanned by  $\text{ADP}^{3-}$ , viz., roughly speaking from the bottom of the cavity to 8  $\text{\AA}$  above it, was divided into two non-overlapping windows, in which up to 60 ns of MD trajectory were generated, thus representing a simulation time of 0.12  $\mu\text{s}$  for the overall reaction pathway.

## Results and Discussion

**Structural Features of *apo*-AAC.** Analysis of the 0.1- $\mu\text{s}$  MD trajectory is depicted in Figure 1. The number density profiles shed light on the organization of *apo*-AAC in the model membrane. They indicate that the carrier is nicely anchored in the lipid environment, its TM helices,  $H_i$ , spanning the width of the hydrophobic core of the bilayer while the short helical stretches,  $h_{ij}$ , appear to be essentially buried in the headgroup region. A glimpse at the opposite leaflet reveals that the mouth of *apo*-AAC emerges slightly below the surface of the model membrane. It is noteworthy that peripheral charged residues of the carrier interact strongly with both the choline and the phosphate moieties of the POPC units.

(25) Andersen, H. C. *J. Comput. Phys.* **1983**, *52*, 24–34.

(26) MacKerell, A. D., Jr.; et al. *J. Phys. Chem. B* **1998**, *102*, 3586–3616.

(27) Feller, S. E.; MacKerell, A. D., Jr. *J. Phys. Chem. B* **2000**, *104*, 7510–7515.

(28) Darve, E.; Pohorille, A. *J. Chem. Phys.* **2001**, *115*, 9169–9183.

(29) Hénin, J.; Chipot, C. *J. Chem. Phys.* **2004**, *121*, 2904–2914.

(30) den Otter, W. K. *J. Chem. Phys.* **2000**, *112*, 7283–7292.

As the simulation of *apo*-AAC proceeds, water molecules from the bulk environment gush into the internal cavity of the membrane protein. Figure 1 illuminates how, within 0.1  $\mu$ s of MD sampling, the hollow structure of the carrier is completely flooded. It is apparent from the number density profiles that the probability to find water molecules across the protein is nonzero and, hence, evocative of a possible communication between the matrix and the IMS of the mitochondria. Such may not be necessarily true, as the computation of number density profiles implies an averaging in the  $x$ - and  $y$ -directions of Cartesian space, normal to the aqueous interface. In reality, a rapid glance at the water isodensity maps of Figure 1 suggests that *apo*-AAC is hermetically close and impervious to the passage of water molecules.

Interestingly enough, flooding of *apo*-AAC is accompanied by the diffusion of chloride counterions toward the wall of the cavity, as highlighted in Figure 1 and in the Supporting Information. On the time scale explored, up to five counterions occupy concomitantly the cavity of the protein, with individual residence times as long as 60 ns. The seven positively charged residues gathered in the lower half of the carrier—viz., R79, R137, R234, R235, R279, K22, and K32—together with those borne by helices H2 and H4, about 10 Å above, in the upper half—viz., K91, K95, K198, and R187—form basic patches toward which the chloride counterions aggregate. Long-lived noncovalent bonds generally correspond to doubly chelated anions interacting with two arginine residues. As will be seen shortly, the asymmetric topological distribution of lysine and arginine amino acids in the cavity is envisioned to enhance the translocation of negatively charged species across the carrier.

Equally remarkable is the fully preserved secondary structure of *apo*-AAC over a period of 0.1  $\mu$ s. As shown in Figure 1, all TM helices,  $H_i$ , and interfacial helical stretches,  $h_{ij}$ , remain unaltered on the time scale explored here. Of particular interest, the  $\alpha$ -helical content of the carrier remains essentially constant, barring sporadic fraying in TM segment H2 over the first 20 ns, which can be legitimately ascribed to partial reorganization of the protein scaffold upon insertion in the POPC bilayer. Overall random coil content is limited, the small loops connecting the TM segments to the interfacial stretches on the matrix side undergoing rapid transition between coil,  $\gamma$ -turn, and  $3_{10}$ - or  $\alpha$ -helical conformations. The marginal distortion of the conformation witnessed on the 0.1- $\mu$ s time scale is consistent with the moderate distance root-mean-square deviation (rmsd) of ca. 2 Å, measured over backbone atoms with respect to the reference PDB 1OKC structure. This value reflects internal motions of reduced amplitude within the TM scaffold resulting from the solvation of the carrier. On the basis of a 10-fold shorter simulation, Falconi et al. reported a somewhat larger distance rmsd of 3 Å,<sup>31</sup> which can be rationalized by the use of a distinct potential energy function.

While the secondary structure of *apo*-AAC is perfectly conserved in the course of the 0.1- $\mu$ s MD simulation, the tertiary structure, however, appears to depart somewhat from that of 1OKC, which features the specific inhibitor CATR. A closer look at the reference crystallographic structure reveals a flared aperture toward both the IMS and the matrix, whereas the *apo* conformation of the carrier has a more pronounced cylindrical shape. In line with this observation, Falconi et al. had previously

underlined that the volume of the internal cavity increased upon removal of the atractyloside. From a structural perspective, alteration of the tertiary structure of *apo*-AAC stems primarily from an inward motion of the C2 loop on the IMS side and of the N-terminus segment and, to a lesser extent, of the C1 loop and of the less flexible C-terminus segment. A decrease in the rigidity of the mitochondrial carrier resulting from the removal of the inhibitor CATR—which can be viewed as a structural wedge—represents a plausible explanation for the displacement of the C2 loop, albeit possible effects of the lipidic environment should not be ruled out.

**Electrostatic Properties of *apo*-AAC.** As has been underlined previously, the two basic patches that line the cavity of the mitochondrial carrier are likely to exert an attractive force onto anions present in the vicinity of the protein, e.g., chloride ions. To understand the relationship between the architecture of the AAC and the net electric forces at play, the electrostatic potential has been mapped numerically in the three dimensions of Cartesian space.<sup>32</sup> Figure 2 illuminates how this quantity varies dramatically between the matrix and the mitochondrial IMS. The conical isopotential surface revealed in this figure is suggestive of a privileged passageway anticipated to guide negatively charged permeants toward the bottom of the carrier, where TM helices H1, H3, and H5 interconnect through salt bridges. Notably, the longitudinal axis of this electrostatic funnel is not rectilinear and, hence, not collinear to the normal to the aqueous interface. Yet, the concept of a favored pathway is not contradictory with the impervious nature of the AAC in its closed conformation brought to light by the water iso-density maps. As illustrated in the contour maps of the electrostatic potential, halfway down the AAC, the concentric isopotential surfaces form a constriction region consistent with the topology of the membrane protein.

The isopotential contour map of Figure 2 indicates that any negatively charged species approaching the mouth of the carrier will be rapidly thrust toward the vestibular space of the latter. In this region, anions can interact favorably with residues K91, K95, K198, and R187 borne by TM helices H2 and H4. To gain further insight into the net electric forces acting on the permeants of the AAC, the electric field has been derived from the three-dimensional maps of the electrostatic potential using the OpenDX open-source visualization package (<http://www.opendx.org>). In the region of interest, where the electrostatic funnel conducts, the intensity of the electric field ranges from ca. 0.075 to 0.125 V/Å. It is apparent that, below the constriction region, the lower basic patch of the cavity causes the direction of the electric field to be reverted. The diphosphate moiety of ADP<sup>3-</sup>, initially pointing upward in the vestibular space, is, therefore, expected to reorient as the permeant sinks down in the crevice of the carrier.

This is demonstrated in the second 0.1- $\mu$ s MD simulation of the AAC with 10 mM ADP and ATP. An ADP<sup>3-</sup> fragment placed below the constriction region at  $t = 0$  undergoes slow reorientation concomitant with its downward diffusion. Figure 2 emphasizes that the diphosphate nucleotide rotates about the central pentose ring, the space swept out by the tilting adenosine- and diphosphate groups being significant. Within ca. 40 ns, the former moiety lands at the bottom of the cavity, roughly parallel to the surface of the lipid bilayer, as the latter associates noncovalently with the positively charged residues of the second basic patch. As will be detailed subsequently, once locked in

(31) Falconi, M.; Chillemi, G.; Di Marino, D.; D'Annessa, B.; Morozzo della Rocca, I.; Palmieri, L.; Desideri, A. *Proteins: Struct. Funct. Bioinf.* **2006**, *65*, 681–691.

(32) Aksimentiev, A.; Schulten, K. *Biophys. J.* **2005**, *88*, 3745–3761.

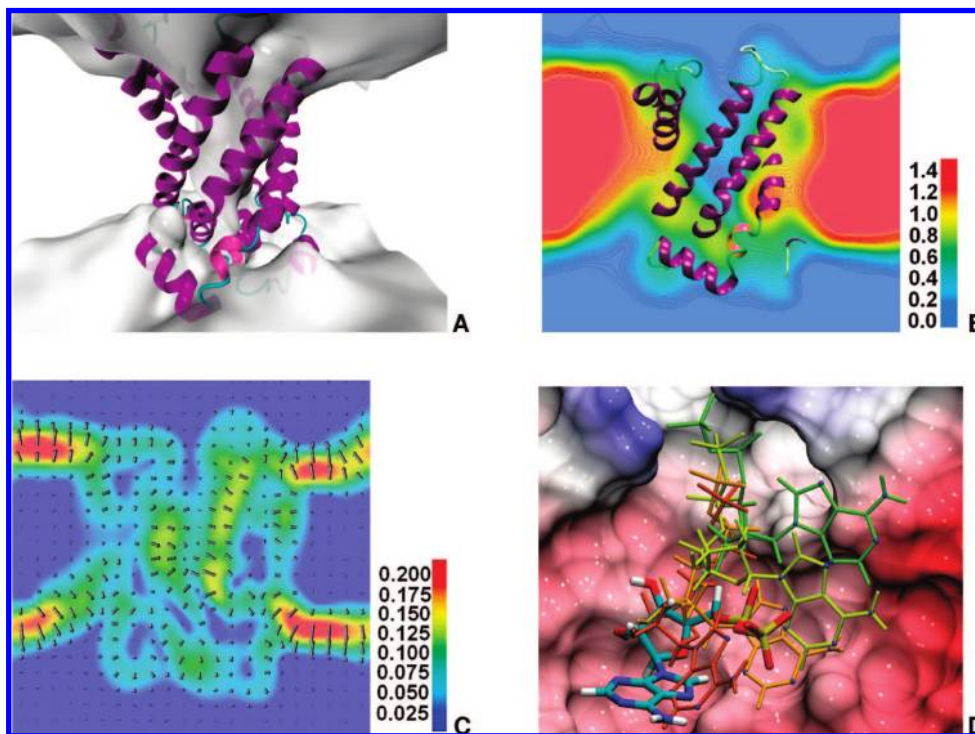


**Figure 2.** (A) Three-dimensional electrostatic isopotential map of *apo*-AAC revealing a funnel conducive to guide  $\text{ADP}^{3-}$  toward the bottom of the closed-state conformation. (B) Electrostatic potential contour maps.<sup>32</sup> Cross-sectional view along the longitudinal axis of the funnel. Values given in units of mV. The contour map was generated with OpenDX (<http://www.opendx.org>). (C) Cross-sectional view of the three-dimensional map of the electric field. The arrows denote the projection of the field in the plane of interest. Values are given in units of mV/Å. (D) Chronological superimposition of  $\text{ADP}^{3-}$  at  $t = 0, 5, 28, 35,$  and  $70$  ns (respectively green, yellow, orange, brown, and colored by element) taken from the  $0.1\text{-}\mu\text{s}$  simulation of AAC with  $10$  mM ADP and ATP. The downward translocation of the permeant in the cavity is accompanied by its tilt, consistent with the local topology of the electric field. The surface of the cavity is colored according to the local value of the electrostatic potential following the coloring scheme of panel B. Orientation of the mitochondrial carrier is identical to that in panels A–C, viz., the longitudinal axis of the protein is collinear with the  $z$ -direction of Cartesian space.

place through an intricate network of salt bridges and hydrogen bonds,  $\text{ADP}^{3-}$  remains frozen in essentially the same orientation and conformation. Legitimately enough, this region of the carrier may be viewed as a binding pocket and the corresponding bound state of the permeant as an intermediary, possibly a recognition pattern, toward its release on the matrix side of the mitochondrial membrane.

**Translocation of  $\text{ADP}^{3-}$  Modifies the Hydrogen-Bond Network of the AAC.** One of the structural signatures of the AAC lies in the possibility to form three salt bridges to interconnect helices H1 to H3, H3 to H5, and H5 to H1.<sup>11</sup> Noncovalent interhelical linkage is achieved through the pairs of residues E29:R137, D134:R234, and D231:K32, which are located in the lower half of the carrier. In the *apo* form of the AAC, it is noteworthy that these salt bridges occur only intermittently (see Figure 3). The most glaring example is D231:K32, which, roughly speaking, satisfies the criteria of a salt bridge only in the first third of the  $0.1\text{-}\mu\text{s}$  MD trajectory. To a large extent, this result is rooted in the original structure, i.e., PDB 1OKC, which was crystallized with specific inhibitor CATR. When setting up the simulation, the latter was removed from the internal cavity of the carrier. It would seem, however, that thermalization of the molecular assay was insufficient to erase the structural lag by allowing the protein scaffold to relax fully upon removal of the glycoside.

Conversely, the simulation of the AAC with  $10$  mM ADP and ATP reveals that the initially broken D134:R234 and D231:K32 salt bridges are restored within  $35$  ns. Yet, whereas the second salt bridge is long-lived, through the remainder of the  $0.1\text{-}\mu\text{s}$  simulation, the first is partially disrupted after ca.  $15$  ns.

This result is not completely surprising, given the more localized positive charge borne by the onium moiety of lysine, compared to the guanidinium functional group of arginine. Barring marginal fluctuations, the E29:R137 salt bridge appears to be essentially preserved throughout the MD trajectory.

The time scale characterizing the formation of the three interhelical salt bridges is congruent with that spanned by the simultaneous diffusion and reorientation of  $\text{ADP}^{3-}$  in the internal cavity of the carrier until locked in place. As the diphosphate nucleotide lands on the bottom of the crevice, it also binds noncovalently positively charged residues of the lower basic patch, viz., K22, R79, and R279. The latter amino acid residues, supplemented by Y186, have been proposed to form the “selectivity filter” of the carrier.<sup>11</sup> It is worth mentioning that site-directed mutagenesis experiments on residues K22 and R79 led to a severely impaired transport of the nucleotide across the mitochondrial membrane.<sup>13</sup>

As highlighted in Figure 3, the resulting salt bridges are established within  $40$  ns, remaining intact for the rest of the simulation. Additional, albeit weaker contacts are also created with N276 and S227 in the form of hydrogen bonds with the adenosine fragment, as well as with I183, primarily of dispersive nature. The ancillary, nonconventional hydrogen bond formed between oxygen atom O3' of the pentose ring and the  $\pi$ -electron cloud of Y186 is also worth underlining, consistent with previous observations in model aqueous- $\pi$  electron interactions.<sup>33</sup>

(33) Suzuki, S.; Green, P. G.; Bumgarner, R. E.; Dasgupta, S.; Goddard, W. A., III; Blake, G. A. *Science* **1992**, *257*, 942.

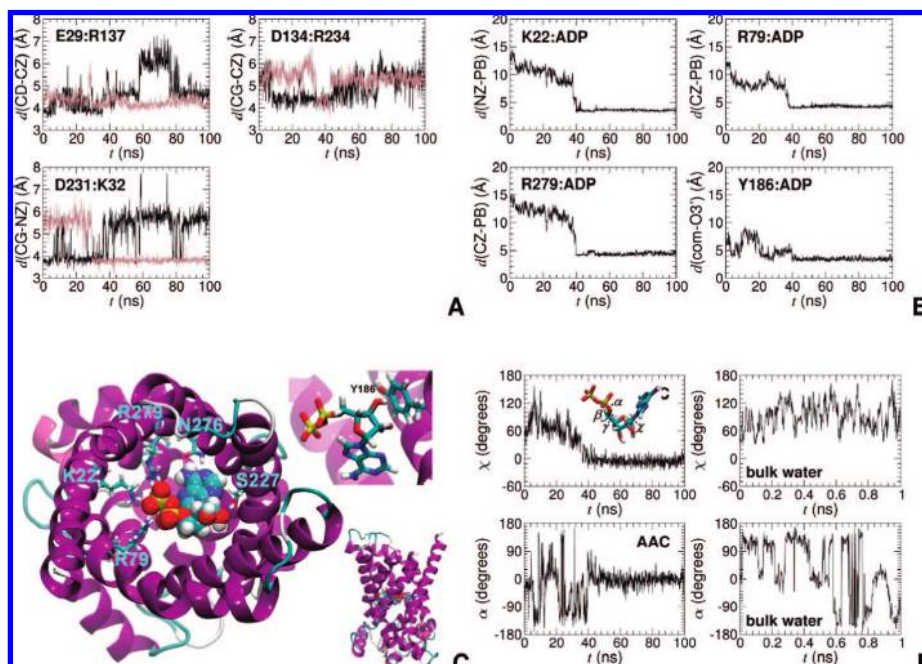


**Figure 3.** (A) Time evolution of the three salt bridges formed between TM helices H1, H3, and H5 in *apo*-AAC (dark lines) and in the assembly formed by AAC with 10 mM ADP and ATP (light lines). (B) Time evolution of the interaction distances between  $\text{ADP}^{3-}$  and key residues of AAC. In the case of Y186, “com” stands for the centroid of the aromatic ring. (C) Detail of the noncovalent bonds formed between  $\text{ADP}^{3-}$  and AAC. The upper inset highlights the pseudo-hydrogen bond established between  $\text{O3}'$  and the  $\pi$ -electron cloud of Y186. (D) Time evolution of representative torsional angles of  $\text{ADP}^{3-}$  locked in AAC (left) and in a bulk aqueous environment (right).  $\alpha$  and  $\chi$  stand for the  $\text{C5}'\text{-O5}'\text{-P-O3}'$  and  $\text{O4}'\text{-C1}'\text{-N9-C8}$  dihedral angles, respectively. Over the 0.1- $\mu\text{s}$  time scale, the adjacent  $\beta$  and  $\gamma$  torsions remain approximately constant around  $180^\circ$  and  $-60^\circ$ , respectively.

The loss of rotational and translational entropy manifested in the binding of  $\text{ADP}^{3-}$  to the mitochondrial carrier is also accompanied by conformational changes in the permeant. Whereas the latter isomerizes rapidly in bulk water—which can be viewed as a naive model of the vestibular space—in particular through its  $\chi$  and  $\alpha$  torsional angles that vary roughly between  $30^\circ$  and  $180^\circ$  and between  $-180^\circ$  and  $180^\circ$ , respectively, it is congealed in the same conformation once locked at the bottom of the crevice. Notably, in the AAC, the diphosphate nucleotide undergoes conformational alterations for approximately the first 40 ns of the complete 0.1- $\mu\text{s}$  trajectory, after which both  $\chi$  and  $\alpha$  remain reasonably close to  $0^\circ$ . Whether in water or in the carrier, the two other dihedral angles,  $\beta$  and  $\gamma$ , plateau around  $180^\circ$  and  $-60^\circ$ , respectively, with only marginal deviation from the latter. That the value of  $\chi$  reached after 40 ns is not sampled in bulk water exemplifies the conformational restraint exerted by the environment on  $\text{ADP}^{3-}$ , reminiscent of the loss of internal degrees of freedom in protein–ligand association.

**Binding of  $\text{ADP}^{3-}$  Is an Early Event of Its Transport across the Inner Membrane.** Simulation of the AAC with 10 mM ADP and ATP suggests that the membrane protein acts as an electrostatic sensor, thrusting the permeant downward along a privileged pathway to reach the bottom of the crevice. Using as a naive reaction coordinate the distance separating the center of mass of  $\text{ADP}^{3-}$  from the centroid of the lower region of helices H1, H3, and H5 projected onto the  $z$ -direction of Cartesian space (see Methods section), the permeant was translocated over the entire 0.1- $\mu\text{s}$  trajectory from 17.3 to 10.4 Å, as shown in Figure 4. If the region of the internal cavity to which  $\text{ADP}^{3-}$  is associated coincides, indeed, with a *true* binding site,<sup>34</sup> a key question, then, remains to be answered: Is

this single experiment reproducible, and would the permeant reach the same binding site upon starting from distinct sets of initial positions and momenta? To tackle this issue, seven independent numerical experiments representing a total simulation time of 0.21  $\mu\text{s}$  were carried out, wherein a single  $\text{ADP}^{3-}$  unit was dropped from different altitudes in the mitochondrial carrier, i.e., different values of the reaction coordinate, and with different orientations.

In the first simulation, the permeant virtually remains at the same altitude over a period of 17.5 ns, viz., approximately 29 Å. Within the first 3.6 ns, the phosphated moiety is anchored to K91, K95, N115, and R187, while the adenosine fragment interacts with Q84, N87, and F88. The subsequent reorientation of  $\text{ADP}^{3-}$  is accompanied by a large-amplitude motion of adenosine, now located above the diphosphate group and interacting with Y194. In the second trajectory, however, the permeant moves down from 33.8 to 27.6 Å within 77 ns, as highlighted in Figure 4. Over the entire simulation, the diphosphate moiety remains anchored to K91, K95, N115, and R187, while adenosine successively forms  $\pi$ -stacking motifs with Y194 and Y190 either individually or together. Throughout this trajectory,  $\text{ADP}^{3-}$  appears to be frozen in a highly strained conformation. Similarly coerced *anti* conformations of the permeants, where the phosphated moiety bends toward the purine ring, have been observed previously in related molecular systems.<sup>35</sup>

In the third experiment, translocation of  $\text{ADP}^{3-}$  proceeds from 33.5 to 21.0 Å over a period of 41 ns. In the first 5.5 ns, its adenosine moiety binds Y194, while the diphosphate fragment interacts with K91. In the remainder of the simulation, the phosphated group interacts sequentially with R187, Y186, and

(34) Robinson, A. J.; Kunji, E. R. S. *Proc. Natl. Acad. Sci. U.S.A.* **2006**, *103*, 2617–2622.

(35) Huber, T.; Klingenberg, M.; Beyer, K. *Biochemistry* **1999**, *38*, 762–769.

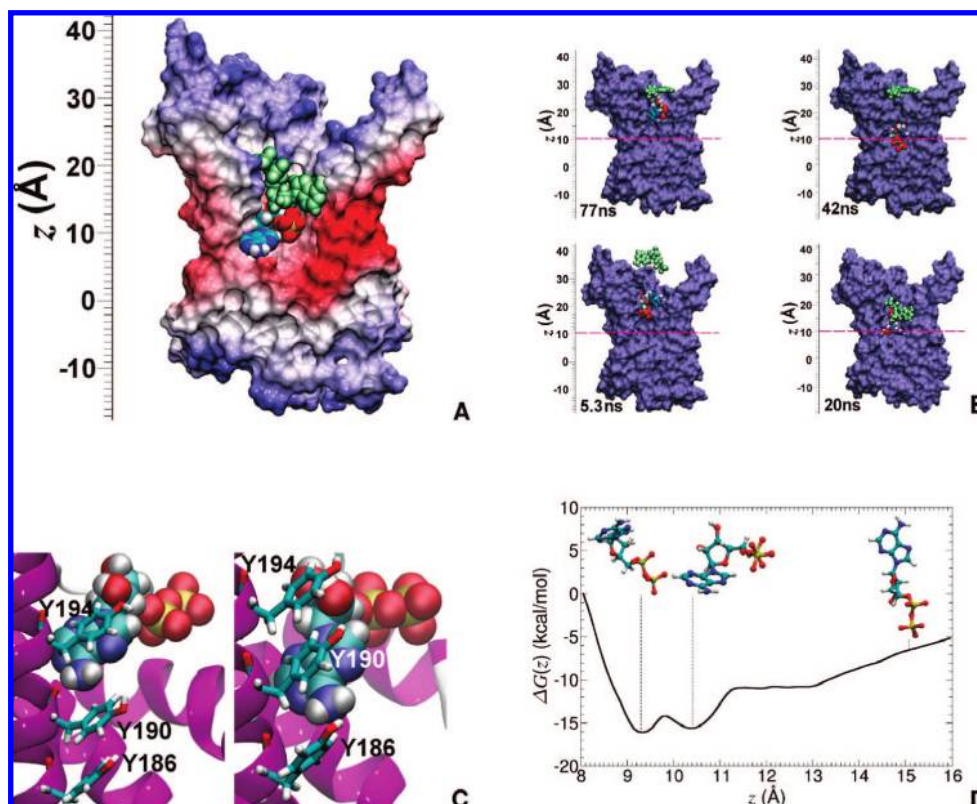


**Figure 4.** (A) Translocation of  $\text{ADP}^{3-}$  in the course of the 0.1- $\mu\text{s}$  simulation of AAC in the presence of ADP and ATP. The initial position of  $\text{ADP}^{3-}$  is featured by pastel green van der Waals spheres. The surface of the carrier is colored according to the local value of the electrostatic potential following the coloring scheme of Figure 2B. (B) Comparison of the trajectories followed by  $\text{ADP}^{3-}$  in different simulations, starting with distinct initial positions and velocities of the permeant: (i) 77, (ii) 42, (iii) 5.3, and (iv) 20 ns. A dashed pink line characterizes the reference equilibrium position of  $\text{ADP}^{3-}$  in the binding pocket of AAC after 0.1  $\mu\text{s}$ . (C) Tyrosine ladder formed by residues Y186, Y190, and Y194, along which  $\text{ADP}^{3-}$  glides, forming sequentially  $\pi$ - $\pi$  stacking interactions with the adenosine moiety. (D) Free energy profile delineating the translocation of  $\text{ADP}^{3-}$  in the cavity of AAC along the  $z$  direction of Cartesian space. The order parameter is the distance separating the center of mass of  $\text{ADP}^{3-}$  from that formed by the lower region of helices H1, H3, and H5, viz., residues 28–37, 133–142, and 230–239, projected onto the  $z$  axis. The insets characterize the conformation of  $\text{ADP}^{3-}$  for different values of the order parameter.  $\text{ADP}^{3-}$  is shown in the orientation of the carrier depicted in panel A.

Y190 as the nucleotide forms long-lived contacts with both N87 and K91. The most significant distance spanned by the permeant is observed in the fourth simulation depicted in Figure 4. Within 42 ns,  $\text{ADP}^{3-}$  moves down from 29.3 to 13.1 Å, gliding along Y194, Y190, and Y186.<sup>11</sup> The diphosphate moiety initially interacts with K22, to which residues R79, R234, and R235 are subsequently added. At the same time, the adenosine fragment, located above the phosphated group, binds R279.

The fifth experiment provides a cogent illustration of the role played by the electrostatic funnel to guide the diphosphate nucleotide toward the hypothesized binding site (see Figure 4). A rapid descent of  $\text{ADP}^{3-}$  from 39.3 to 22.8 Å is witnessed over 5.3 ns. Here again, the adenosine moiety appears to interact successively with the tyrosine ladder formed by residues Y186, Y190, and Y194. The permeant is essentially collinear to the longitudinal axis of the carrier, its diphosphate group pointing downward, ultimately interacting with R187 and K91. In sharp contrast, the sixth simulation reveals that the adenosine moiety is below the phosphated group. Over 3.6 ns, the permeant is translocated from 39.2 to 28.8 Å. The nucleotide interacts preferentially with K91, K95, and N87.

For the seventh and last numerical experiment, the starting position of  $\text{ADP}^{3-}$  is roughly similar to that chosen in the aforementioned reference, 0.1- $\mu\text{s}$  simulation, the initial set of velocities being different. As shown in Figure 4, within 20 ns, the permeant moves down from 17.3 to 11.5 Å, the adenosine moiety tilting in a sweeping motion comparable to that observed

in the longer, 0.1- $\mu\text{s}$  trajectory (see Figure 2), eventually interacting with R79, R234, R235, and D134, while the diphosphate group binds K91.

Put together, the seven independent MD simulations described here illustrate the pronounced sensitivity of the investigated phenomenon to the chosen initial conditions, in particular, over the admittedly limited time scales being explored. They also underscore the complementary roles of electrostatic probe and electrostatic sensor, played respectively by the permeant and the mitochondrial carrier, accounting for the rapid attraction of  $\text{ADP}^{3-}$  toward the bottom of the crevice. Inappropriate initial orientation and conformation of the permeant can, however, lead to an equally rapidly hampered diffusion across the AAC,  $\text{ADP}^{3-}$  being generally trapped in the constriction region, where it is congealed in an inert conformation and forms long-lived interactions with its environment. To address the issue of quasi-nonergodicity exemplified in these numerical experiments and, most importantly, reconcile the latter with the free energy landscape that characterizes the transport of the permeant in the mitochondrial carrier, additional simulations were performed using the ABF method.<sup>28,29</sup>

The free energy profile of Figure 4 delineates the translocation of  $\text{ADP}^{3-}$  in the carrier, roughly speaking from the constriction region to the bottom of the internal cavity, hence covering a range of 8 Å of the order parameter. However naive this order parameter may be—the *true* reaction coordinate being in all probability a multidimensional one—it nonetheless provides a

compelling evidence that the binding site brought to light in the 0.1- $\mu$ s MD trajectory corresponds to a minimum of the free energy. As has been discussed above, this minimum emerges at ca. 10.4 Å and is characterized by the adenosine moiety of ADP<sup>3-</sup> lying flat on the bottom of the crevice, while the diphosphate group forms an intricate network of salt bridges with residues K22, R79, and R279.

An interesting feature revealed by the present free energy calculations is the existence of a second minimum, found slightly deeper in the carrier, at ca. 9.3 Å. What distinguishes the two minima of comparable depth and separated by a barrier of less than 2 kcal/mol lies essentially in the orientation of ADP<sup>3-</sup>. Whereas over the 0.1- $\mu$ s time scale of the MD trajectory, it remained locked in the same position after 40 ns, ABF allows, through reversible diffusion, its reorientation and isomerization, predominantly about the  $\chi$  and  $\alpha$  dihedral angles. The permeant, initially located at ca. 10.4 Å, rotates about its pentose ring, so that the adenosine fragment, initially beneath it, is now above, pointing toward the vestibule, while the diphosphate group penetrates deeper down in the cavity. This new conformation is conducive to an enhanced induced fit, mirrored in a somewhat lower ADP:AAC interaction energy (see Supporting Information). Contrasting with the reference 0.1- $\mu$ s MD simulation, the free energy minimum found at 9.3 Å corresponds to a disrupted D231:K32 salt bridge.

A number of previously published data appear to corroborate this result. In particular, residues pertaining to the MCF motif of the yeast carrier have been systematically mutated, and the function of the mutants investigated. Among the mutations of the six residues corresponding to the bovine residues, viz., E29,<sup>36,37</sup> K32,<sup>37</sup> D134,<sup>12,37</sup> R137,<sup>37</sup> D231,<sup>37</sup> and R234,<sup>36,38,39</sup> two main observations were made. First, the residues that have proven to be the most sensitive to inhibitor ATR, CATR, and BA binding and to nucleotide exchange are K32, D134, and D231; i.e., mutations of equivalent residues in yeast lead to almost no binding for ATR or CATR and BA and almost no nucleotide exchange. Second, when mutations are carried out on yeast residues equivalent to K32, D231, and R234, no second-site revertants are detected. The latter suggests that the function cannot be recovered easily and that these residues are likely to play an important role in the mitochondrial function. Put together, these results underscore the importance of the two residues forming salt bridge D231:K32.

In contrast with the latter salt bridge, E29:R137 is only partially preserved through the sole noncovalent interaction of the OE1 oxygen atom with the hydrogen atoms borne by NH2. Compared with the 10.4-Å minimum, the lower position of ADP<sup>3-</sup> in the carrier promotes a strong interaction of the phosphated moiety with R137.

The region of the mitochondrial carrier that encompasses the two minima is prefaced in both directions by large free energy barriers. Not too surprisingly, the steeper barrier corresponds to the bottom of the crevice, which has been shown to be impervious to the passage of small chemical species, like water molecules (see Figure 1). It may be anticipated that brute-force

translocation of ADP<sup>3-</sup> below 9.3 Å would require a considerable positive work imposed by the structural rearrangement of the TM helices, which evidently is not amenable to classical MD simulations. The barrier arising above 10.4 Å reflects the energetic cost incurred for disrupting the noncovalent bonds formed between the permeant and its binding site. The free energy plateau that follows within the next ca. 2 Å is suggestive of an unhampered translocation and isotropic orientation of the permeant. Beyond 13 Å, the free energy increases again as the diphosphate nucleotide crosses the constriction region of the carrier. It is noteworthy that, in these ABF calculations, the phosphated moiety is systematically predicted to point downward, i.e., in the direction of the lower basic patch, which is congruent with the conclusions drawn from the above independent numerical experiments.

## Conclusions

The early events of ADP transport across the mitochondrial AAC<sup>11,13</sup> have been examined based on large-scale MD simulations. Investigation of *apo*-AAC confirms the impervious nature of the carrier, which prevents the exchange of chemical species between the matrix and the IMS of the mitochondria. Simulation in a model membrane over the 0.1- $\mu$ s time scale underscores the robustness of the  $\alpha$ -helical TM scaffold. Three-dimensional mapping of the electrostatic potential brings to light a privileged, funnel-like passageway envisioned to drive rapidly permeants toward the bottom of the membrane protein. Mirroring the distinctive distribution of charged amino acids in the carrier, the revolving directionality of the electric field is suggestive of a possible reorientation of the permeant as the latter descends in the internal cavity.

0.1- $\mu$ s simulation of AAC with 10 mM ADP and ATP reveals a possible recognition site for ADP<sup>3-</sup> at the bottom of this cavity. The loss of orientational and conformational entropy of the permeant as it binds the crevice is reminiscent of protein–ligand association. Additional independent numerical experiments, wherein ADP<sup>3-</sup> is dropped at different altitudes in the mitochondrial carrier, illustrate over the time scales explored the marked sensitivity of the process to the chosen starting positions and momenta. The rationale for probing different starting points stems from our limited knowledge of how the nucleotide approaches the AAC, in particular what is the preferred orientation and conformation of the substrate at a given separation from the mouth of the transporter. Assuming appropriate orientation, the diphosphate nucleotide is thrust downward, reaching rapidly the hypothesized binding region of the carrier. Conversely, under inadequate initial conditions, ADP<sup>3-</sup> may remain frozen in a kinetic trap, systematically near the constriction region of the AAC. While the present results do not necessarily imply that the path followed by the permeant is unique, it may be legitimately inferred that, if the transport phenomenon is witnessed on an appreciably short time scale, e.g., 42 ns to cover approximately 16 Å, the corresponding trajectory is thermodynamically relevant. It may further be contended that, given the limited time scale over which it is monitored, translocation of ADP<sup>3-</sup> is a highly probable event. That the substrate does not reach the postulated binding site, down in the crevice, simply means that sampling is incomplete.

The proposed binding site highlighted in the present classical MD simulations, and identified from structural analyses based on sequence similarities,<sup>34</sup> is shown to correspond to a true minimum of the free energy landscape determined along the longitudinal axis of the membrane protein, employing an

(36) Klingenberg, M.; Nelson, D. R. *Biochim. Biophys. Acta* **1994**, *1187*, 241–244.

(37) Müller, V.; Heidkämper, D.; Nelson, D. R.; Klingenberg, M. *Biochemistry* **1997**, *36*, 16008–16018.

(38) Nelson, D. R.; Lawson, J. E.; Klingenberg, M.; Douglas, M. G. *J. Mol. Biol.* **1993**, *230*, 1159–1170.

(39) Heidkämper, D.; Müller, V.; Nelson, D. R.; Klingenberg, M. *Biochemistry* **1996**, *35*, 16144–16152.

adaptive biasing scheme. The resulting free energy profile features two neighboring minima of comparable depth, which characterize distinct binding modes and orientations of  $\text{ADP}^{3-}$ , thereby lending support to the hypothesis of a true association site put forth on the basis of the crystallographic structure.<sup>11</sup> The 10 kcal/mol free energy difference between these minima and the constriction region rationalizes the fast downward translocation of the diphosphate nucleotide. In the opposite direction, the steep free energy barrier encountered by  $\text{ADP}^{3-}$  as it moves farther down the mitochondrial carrier is congruent with the accepted view of an impermeable carrier impeding further progression of the permeant toward the mitochondrial matrix.

The set of simulations reported here emphasizes that the rapid binding of  $\text{ADP}^{3-}$  to the internal cavity of the AAC constitutes an early event of its transport across the inner membrane, known to span the millisecond time scale.<sup>40</sup> Recognition of the diphosphate nucleotide and association thereof with the mitochondrial carrier is hypothesized to trigger the opening of the latter, an event anticipated to span significantly longer time scales. Opening could occur through the triplet of proline residues P27, P132, and P229, which act as hinges in helices H1, H3, and H5, respectively. Paradoxically, binding of  $\text{ADP}^{3-}$  to the AAC is accompanied by the formation of salt bridges between these three TM segments, a process envisioned to reinforce the  $\alpha$ -helical scaffold rather than disrupt it into a conformation opened toward the matrix.

This apparent paradox is, however, removed when considering the free energy minimum pinpointed at 9.3 Å, employing ABF calculations. Whereas binding of  $\text{ADP}^{3-}$  to the crevice initially strengthens the bundle of TM helices through the creation of interhelical salt bridges, subsequent reorientation and isomerization of the permeant as it moves deeper down in the carrier ruptures the observed network of noncovalent bonds. This disruption could be viewed as a preamble to the opening of the membrane protein toward the matrix of the mitochondria,

albeit an atomic-level description of the complete transport phenomenon, which is likely to embrace both environment-dependent processes and events of stochastic nature, currently remains out of reach. It is, nevertheless, reasonable to believe that, as novel experimental advances are published, theoretical approaches will be used profitably to gain additional insight into the mechanisms that underlie the assisted passage of nucleotides across the mitochondrial membrane.

Such experimental advances imply the design of new blocking agents targeted at trapping intermediate structures that represent potential milestones of the transport process. De novo design of analogues solely in the light of a single crystallographic structure has, however, proven to be a difficult undertaking. In the present work and for the first time, the interaction of the substrate with the mitochondrial carrier is revealed at the atomic level over the initial stage of the translocation pathway. Contacts formed between key residues of the AAC and both the adenosine and the phosphate moieties of  $\text{ADP}^{3-}$  provide valuable guidance for the rational modification of the substrate or the design of site-directed mutagenesis experiments on the membrane protein.

**Acknowledgment.** The authors are indebted to Emad Tajkhorshid for insightful discussions. The Centre Informatique National de l'Enseignement Supérieur (CINES), Montpellier, France, and the Centre de Calcul, Recherche et Technologie (CCRT), Arpajon, France, are gratefully acknowledged for generous provision of computational time. This work is funded by the Agence nationale pour la recherche (ANR).

**Supporting Information Available:** Figures showing the structure of the ADP/ATP mitochondrial carrier, the mass-weighted isodensity map and residence time of the chloride counterions in *apo*-AAC, interaction energy of  $\text{ADP}^{3-}$  with the mitochondrial carrier from classical MD and ABF calculations, complete ref 26, and an AVI movie generated from the 42-ns numerical experiment, during which  $\text{ADP}^{3-}$  was dropped near the mouth of the mitochondrial carrier. This material is available free of charge via the Internet at <http://pubs.acs.org>.

JA8033087

(40) Gropp, T.; Brustovetsky, N.; Klingenberg, M.; Müller, V.; Fendler, K.; Bamberg, E. *Biophys. J.* **1999**, *77*, 714–726.

(41) Humphrey, W.; Dalke, A.; Schulten, K. *J. Mol. Graphics* **1996**, *14*, 33–38.